Charge-discharge properties and reaction mechanism of cation-disordered rutile-type $Li_{1.2}MnFe_{1.2}F_{6.8}$

Yayun Zheng, Jinkwang Hwang, Kazuhiko Matsumoto*, Rika Hagiwara

Graduate School of Energy Science, Kyoto University, Yoshida-Honmachi, Sakyo-ku, Kyoto 606-8501, Japan

*Corresponding author: Kazuhiko Matsumoto

E-mail: k-matsumoto@energy.kyoto-u.ac.jp

Tel: +81757534817

Fax: +81757535906

ABSTRACT

A carbon-coated $Li_{1.2}MnFe_{1.2}F_{6.8}$ with a cation-disordered rutile structure is presented for the first time as a positive electrode material for lithium-ion batteries. For improved performance, the composite electrode is investigated at 90 °C using a thermally stable ionic liquid electrolyte. A combination of synchrotron X-ray diffraction, X-ray photoelectron spectroscopy and half-cell tests establish that the reversible extraction/insertion of lithium from/into $Li_{1.2}MnFe_{1.2}F_{6.8}$ in the 2.5–4.5 V voltage range at 90 °C involves Fe(III)/Fe(II) and Mn(III)/Mn(II) redox reactions alongside partial conversion reactions between the rutile $Li_{1.2}MnFe_{1.2}F_{6.8}$ and a mixture of LiF and rutile FeF_2. Deep discharge to 2.0 V involves a conversion reaction to LiF and metallic Fe and Mn accompanied by the partial preservation of the rutile structure.

Graphical abstract

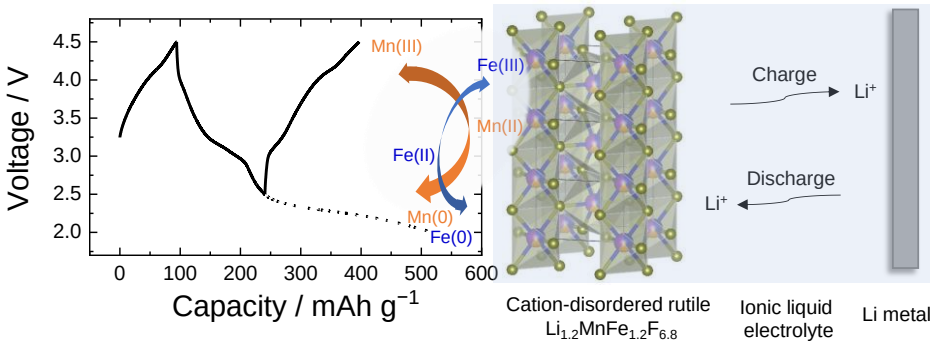

Highlights

- Preparation of a cation-disordered rutile-type $Li_{1.2}MnFe_{1.2}F_{6.8}$.
- Electrochemical performance improvement in an ionic liquid electrolyte at 90 °C.
- Reaction mechanism analysis through ex-situ synchrotron X-ray diffraction.
- Topotactic and conversion reactions in high and low voltage ranges, respectively.

Keywords

Cation-disordered rutile structure, Li^+ extraction/insertion, conversion reaction, redox activities

1. Introduction

Transition metal fluorides, renowned for their superior output voltages attributed to the high electronegativity of fluorine and high theoretical capacity including conversion reactions, have been acclaimed as viable alternatives to transition metal oxide positive electrode materials for lithium-ion batteries (LIBs) [1-6]. Within electrode materials based on transition metal fluorides in previous works, iron fluoride systems were most widely studied both by experimental and theoretical techniques [4, 7-17]. Mixing of metal ions sometimes withdraws favorable performance of electrode materials from various aspects. In this context, the trirutile-type (rutile-type when disordered) positive electrode materials provide a good structural frame of fluoride materials. Most Li*M*(II)*M*(III)F_6–type fluorides (where *M*(II) = Fe, Co, Mg, Ni, Cu; *M*(III) = Fe, Cr, Ga) have been reported to embody the trirutile structure which has been identified in compounds such as $LiCoCrF_6$, $LiCoFeF_6$, and $LiFe_2F_6$ [18-20]. The trirutile Li*M*(II)*M*(III)F_6 structure, which belongs to the tetragonal space group $P4_2/mnm$, typically comprises LiF_6, *M*(II)F_6, and *M*(III)F_6 octahedra. The metal fluoride octahedra share edges along the *c* direction and corners in the *ab* plane, leaving tunnels along the *c* axis to facilitate Li^+ transport in this direction. Some compounds in the Li*M*(II)*M*(III)F_6 family have also been noted to adopt a rutile structure that is almost identical to the trirutile structure except for the Li^+, *M*(II), and *M*(III) ions which tend to be disordered with random occupancy of metal positions in the rutile structure [21, 22].

Although the preparation and structural characterization of trirutile and rutile Li*M*(II)*M*(III)F_6 compounds are well-established in literature stemming back to early 1970s, inquests into their application as LIBs positive electrode materials are comparatively recent. Table 1 presents a summary of the electrochemical properties of selected Li*M*(II)*M*(III)F_6 positive electrodes for LIBs. For instance, a study by Liao et al. reported the cation-disordered rutile-type $LiFe_2F_6$ and $LiMgFeF_6$, where all the cations are disordered. Here, the rutile $LiFe_2F_6$

showed that the reversible insertion of Li^+ occurred within the $Li_{1+x}Fe_2F_6$ ($0 < x < 0.6$) tunnels in a single-phase manner, whereas $LiMgFeF_6$ was found to be electrochemically inactive [21, 22]. In a subsequent study by Lieser et al., a cation-ordered trirutile $LiMgFeF_6$ electrode synthesized through a sol-gel process exhibited enhanced electrochemical properties marked by a reversible specific capacity of 107 mAh g^{-1} [23]. Other studies on the charge-discharge behavior of trirutile $LiNiFeF_6$ have reported Li^+ insertion to occur via a phase separation mechanism between Li-lean $Li_{1+x1}NiFeF_6$ and Li-rich $Li_{1+x2}NiFeF_6$ ($x1 \leq 0.16 \leq x2$) where the trirutile structure was preserved [24, 25]. Also, in a bid to expound on this subject, we recently reported an ordered trirutile $LiFe_2F_6$ (also expressed as $Li_{0.5}FeF_3$) obtained by heat treating a ball-milled equimolar mixture of LiF, FeF_2, and FeF_3 [26]. Synchrotron XRD analyses noted that the trirutile $LiFe_2F_6$ structure facilitated a reversible insertion/extraction of Li^+ via a two-phase reaction in the voltage range of 3.2−4.3 V. Our study further revealed that in the lower voltage range of 2.5−3.2 V, a conversion reaction from the trirutile $LiFe_2F_6$ to a mixture of rutile FeF_2 and rock-salt LiF occurred instead of the formation of Li-rich $Li_{1+x}Fe_2F_6$ [26].

It is worth noting that lithium transition metal fluorides do not exclusively crystallize in the trirutile structure. Depending on the arrangement of the different valence metal cations in the octahedral sites, other structures such as the trigonal colquiriite-type ($P\bar{3}1c$) and the Na_2SiF_6-type ($P321$) structures have also been reported among certain Li*M*(II)*M*(III)F_6 (where *M*(II) = Ca, Mn; *M*(III) = Fe, Ga) compositions [27-29]. The trigonal colquiriite-type structure, exemplified in a zero-strain $LiCaFeF_6$ [29], has spatially distributed cations occupying distorted octahedral environments between planes of closest-packed fluoride anions extending in the *ab* plane. On the other hand, the Na_2SiF_6-type structure, which is manifested in $LiMnFeF_6$ [28], comprises SiF_6 units sharing three edges with NaF_6 octahedra, forming empty zigzag channels that facilitate lithium diffusion. As expected, these structural differences give rise to different cycle performances during electrochemical operations. For example, $LiCaFeF_6$

exhibits good cycle performance with minimal changes in the lattice structure[29]. whereas $LiMnFeF_6$ delivers a poor performance because the Li-rich $Li_{1+x}MnFeF_6$ undergoes a phase transition from the Na_2SiF_6-type to rutile-type structure [28]: which effectively rearranges the FeF_6 octahedra connectivity. Reports by Sekino et al. have shown that such phase transformations (*i.e.,* Na_2SiF_6-type Li*M*(II)*M*(III)F_6 to rutile-type or trirutile-type structures) can be induced by changes in compositions, pressure, and temperature (e.g. $(Li, Ti)_{1-x}Co_{1+2x}F_6$, $LiNi_{1-x}Mn_xCrF_6$) [28, 30].

Given the detrimental effects of the Na_2SiF_6-type to rutile-type structural transformations in $LiMnFeF_6$ [28], we postulate that electrochemical performance can be improved by substituting it with a rutile-type $Li_xMn_yFe_zF_6$ to circumvent the unfavorable phase transitions. Therefore, in a bid to validate this hypothesis, we report for the first time, the preparation of a Li-rich $Li_{1.06}Mn_{0.88}Fe_{1.06}F_6$ phase (hereafter, denoted as $Li_{1.2}MnFe_{1.2}F_{6.8}$) with a cation-disordered rutile structure as a positive electrode for LIBs. Here, we explore the electrochemical properties and reaction mechanism(s) of the positive electrode material at elevated temperatures with the aid of a thermally stable ionic liquid (IL) electrolyte to bring out the electrochemical capabilities of the positive electrode material [31-33]. Additionally, the electrochemical behavior of the composite electrode is explicated in detail using synchrotron X-ray diffraction (XRD) and X-ray photoelectron spectroscopy (XPS) analyses.

2. Experimental

2.1. Materials and Treatment

All nonvolatile materials were handled under an Ar atmosphere in a glovebox. All metal fluorides were dried under vacuum at 120 °C in order to remove the moisture before storing in the glovebox. Tetrahydrofuran (THF; dehydrated, Wako Pure Chemical Industries, water content < 10 ppm, stabilizer-free) was used as supplied. Lithium metal (Sigma-Aldrich, 99.95%) was used by cutting off its surface and separating a fresh part with a knife. The FSA salts, Li[FSA] (FSA^-: bis(fluorosulfonyl)amide anion, Kishida Chemical, water content < 20 ppm) and [C_2C_1im][FSA] ($C_2C_1im^+$: 1-ethyl-3-methylimidazolium, Kanto Chemical, water content < 20 ppm), were dried under vacuum at 90 °C prior to use.

2.2.Target material preparation

In the first step for preparing carbon-coated $Li_{1.2}MnFe_{1.2}F_{6.8}$, LiF (Sigma-Aldrich, purity > 99.99%), MnF_2 (Sigma-Aldrich, purity > 98%), and FeF_3 (Sigma-Aldrich, purity > 97%) were mixed in a molar ratio of 1.2 : 1 : 1.2. The mixed powder (~1 g) was loaded in an airtight vessel with a zirconia inner wall under a dry argon atmosphere. The mixture was then ball-milled in a planetary ball mill (Planetary Micro Mill PULVERISETTE 7 premium line, Fritsch) at 800 rpm for 24 h with zirconia balls (3 mm in diameter, 30 g). The pink powder was recovered from the bowl in the glovebox. In the second step, the collected powder was mixed with acetylene black (AB; Wako Pure Chemical Industries, purity > 99.99%) in a weight ratio of 75:25 through ball-milling for 1 h at 800 rpm.

2.3 Electrode and cell preparations

The electrode sheet was prepared by thoroughly mixing the carbon-coated $Li_{1.2}MnFe_{1.2}F_{6.8}$ with poly(tetrafluoroethylene) binder (PTFE; Sigma-Aldrich, Inc.; particle size: ca. 200 μm) at

a ratio of 95:5 using an agate mortar and a pestle. The test electrode was finally obtained by pressing the electrode sheet on fresh Al mesh (13 mm in diameter) with a loading mass of ~2 mg cm^{-2}. The ionic liquid (IL) electrolyte was prepared thoroughly stirring the mixture of Li[FSA] and [C_2C_1im][FSA] with a molar ratio of 40:60. Coin cells (2032-type) were assembled in the Ar-filled glovebox with the $Li_{1.2}MnFe_{1.2}F_{6.8}$ working electrode, the Li[FSA]-[C_2C_1im][FSA] (40:60 in mol) IL electrolyte, and the Li metal disk counter electrode fixed on a stainless steel (SUS316L) plate current collector. The glass microfiber separator (Whatman, GF/A; 16 mm in diameter and 260 μm in thickness) was immersed in the IL electrolyte under vacuum at 90 °C for 12 h prior to cell assembling. All the electrochemical data were obtained by an HJ-SD8 charge−discharge system (Hokuto Denko). The charge−discharge curves and cycling performance of the working electrode were measured by galvanostatic charge−discharge tests.

2.4 Analysis

The XRD pattern of the final compound carbon-coated $Li_{1.2}MnFe_{1.2}F_{6.8}$ was recorded in the Bragg−Brentano geometry using a Rigaku MiniFlex diffractometer with Ni-filtered Cu*K*α radiation (30 kV and 10 mA) and a D/tex Ultra250 Si-strip high-speed detector. Structural parameters were refined with the Rietveld refinement by curve-fitting using the GSAS data analysis software [34]. The crystal structure was visualized by the VESTA program [35]. Synchrotron XRD patterns of the $Li_{1.2}MnFe_{1.2}F_{6.8}$ electrodes at different states of charge were recorded in the BL5S2 of the Aichi Synchrotron Radiation Center equipped with a PILATUS 100 K two-dimensional detector with a wavelength of 0.88589 Å. The electrode powders washed with THF and vacuum-dried at room temperature were sealed in Lindeman glass capillaries. The XPS analysis of the $Li_{1.2}MnFe_{1.2}F_{6.8}$ electrodes at different states of charge were carried out using a JEOL JPS-9010 XPS instrument with Mg*K*α radiation (λ = 9.89 Å, 10

kV−10 mA) after Ar etching at an ion energy of 400 eV for 30 s. The obtained spectra were analyzed using analytical software (SpecSurf, ver. 1.8.3.7, JEOL, Ltd).

3. Result and Discussion

3.1.Crystal structure

A carbon-coated $Li_{1.2}MnFe_{1.2}F_{6.8}$ working composite was prepared via a two-step ball-milling process. This composition was selected out of several other compositions in a preliminary screening to avoid the possible formation of byproducts such as Li_3FeF_6. Fig. 1 shows the XRD pattern of the final composite, which was obtained to ascertain the structure of $Li_{1.2}MnFe_{1.2}F_{6.8}$ crystalline phase in the composite. The obtained XRD data established the absence of any residual starting material (LiF, MnF_2, or FeF_3) or the byproduct Li_3FeF_6 phase in the carbon-coated $Li_{1.2}MnFe_{1.2}F_{6.8}$ (Fig. 1a). Even though the detailed structural analysis is prevented by the broad diffraction peaks, the calculated pattern (red line), which is obtained by Rietveld refinement based on a rutile phase with all the metal cations occupying the 2*a* site (Fig. 1a and Table S1), is congruent with the experimental XRD pattern (black line). Compared to the ordered trirutile $LiFe_2F_6$ [26], the obtained $Li_{1.2}MnFe_{1.2}F_{6.8}$ can be characterized as a rutile structure wherein all cations are disordered in their stoichiometric occupancies in the 2*a* site (Fig. 1b).

3.2. Charge-discharge properties

The electrochemical properties of a Li/$Li_{1.2}MnFe_{1.2}F_{6.8}$ half-cell containing Li[FSA]-[C_2C_1im][FSA] (40:60 in mol) IL electrolyte were investigated at room temperature (25 °C), and elevated temperature (90 °C) to determine the effect of temperature on the charge-discharge behavior of the $Li_{1.2}MnFe_{1.2}F_{6.8}$ electrode. The temperature of 90 °C is suitable to improve battery performance using thermally stable ILs without introducing special peripheral materials,

whereas most organic electrolytes (and solid-electrolyte interphase from organic electrolytes) are unstable at this temperature. The electrode manifested a limited initial discharge capacity of 63 mAh g^{-1} at 25 °C with poor electrochemical activity observed across 30 cycles (Fig. S1a and b). Conversely, the electrode demonstrated improved performance at 90 °C (Fig. 2), emphasizing the vital role of elevated temperatures and the necessity of a thermally stable IL electrolyte to activate $Li_{1.2}MnFe_{1.2}F_{6.8}$ capabilities [36-39]. As such, the charge-discharge behavior of the $Li_{1.2}MnFe_{1.2}F_{6.8}$ electrode at 90 °C was investigated in the voltage range of 2.5–4.5 V at 23.1 mA g^{-1}, as shown in Fig. 2a. The initial charge to 4.5 V delivered a capacity of 94 mAh g^{-1}, corresponding to a ~0.91 Li^+ extraction (based on its theoretical capacity (103 mAh g^{-1}) equivalence to 1.0 Li^+ extraction from $Li_{1.2}MnFe_{1.2}F_{6.8}$). The initial discharge to 2.5 V resulted in a 146 mAh g^{-1} capacity, which notably exceeds the abovementioned theoretical capacity of 1.0 Li^+ transfer. This capacity surplus evinces the occurrence of a conversion reaction that most likely ensues below 2.9 V, where a change in the gradient of the discharge curve was noted (Fig. 2a and b). The rationale behind this behavior will be discussed later with XRD and XPS results. Continued cycling in the 2.5–4.5 V voltage range engendered charge-discharge curves with gentle plateaus around 4.1 V and 3.0 V during charge and discharge, respectively (see dQ/dV plot in Fig. 2b). The first 10 cycles were marked by a gradual increase in discharge capacity, followed by a steady decrease over the subsequent 30 cycles (see cycling performance in Fig. 2c and d). Over the 40 cycles, an average coulombic efficiency of 102.6% was achieved, along with a discharge capacity of 115 mAh g^{-1} at the 40th cycle. These results suggest that the partial conversion reaction induces different redox activities that increase the discharge capacity of $Li_{1.2}MnFe_{1.2}F_{6.8}$ over the first 10 cycles but cause a gradual electrode degradation that diminishes the discharge capacity thereafter. The charge-discharge profiles with pre-discharge measured in this voltage was also investigated (Fig. S2). Pre-discharge to 2.5 V delivered a capacity around 59 mAh g^{-1} with a gentle plateau around 3.0 V, which

corresponds to a conversion reaction involving the reduction reaction of Fe(III)/Fe(II). The subsequent cycles provided the same charge-discharge curves as that measured without pre-discharge (Fig. 2), indicating two redox reactions Fe(III)/Fe(II) and Mn(III)/Mn(II) are involved after the pre-discharge in the cut-off voltage of 2.5−4.5 V.

In order to examine the effects of a complete conversion reaction on the electrochemical properties of the $Li_{1.2}MnFe_{1.2}F_{6.8}$ electrode, the lower cut-off voltage limit was extended to 2.0 V. Charge-discharge curves were obtained in the voltage range of 2.0–4.5 V as illustrated in Fig. 3a. The initial discharge to 2.0 V was characterized by a long plateau around 2.3 V, attaining a capacity of 417 mAh g^{-1} (Fig. 3a and b). This discharge capacity corresponds to 4.0 Li^+, wherein 1.0 Li^+ was obtained through insertion and 3.0 Li^+ from the conversion reaction to zero-valent transition metal. The high electrochemical activity of the $Li_{1.2}MnFe_{1.2}F_{6.8}$ electrode between 2.0–4.5 V is considered to be brought out by elevated temperature (90 °C) with the aid of Li[FSA]-[C_2C_1im][FSA] (40:60 in mol) IL electrolyte. During the subsequent cycles, the discharge capacity was observed to progressively decline to 257 mAh g^{-1} at the 10th cycle, accompanied by the disappearance of the long sloping plateau around 2.3 V (Fig. 3c and d), which evidences that the conversion reaction to zero-valent transition metal is poorly reversible. Compared with some Li*M*(II)*M*(III)F_6-type positive electrode materials listed in Table 1, especially Na_2SiF_6-type $LiMnFeF_6$, the rutile $Li_{1.2}MnFe_{1.2}F_{6.8}$ electrode shows a higher discharge capacity in the same voltage range (2.0–4.5 V), even in a narrow voltage range (2.5–4.5 V) and higher rate (23.1 mA g^{-1}). However, long-term cycling of the rutile $Li_{1.2}MnFe_{1.2}F_{6.8}$ electrode was hindered in the two different voltage ranges owing to the limited reversibility of the conversion reaction, which was also observed from the similar family of materials in previous works (see Table 1). Nevertheless, the exploration of its reaction mechanism provides important information to discover the origins of the poor performance and further explore the family of structurally related materials with improved performance. The pre-discharge to 2.0

V was also characterized by a long plateau around 2.3 V with a capacity of 314 mAh g^{-1}, involved in the conversion reaction to metallic Fe (Fig. S3). The subsequent charge-discharge tests also provided capacities close to that obtained without pre-discharge (Fig. 3), accompanied by the nearly identical charge-discharge curves. All these electrochemical data suggest that rutile $Li_{1.2}MnFe_{1.2}F_{6.8}$ can be initially charged or discharged, and the initial charge-discharge direction does not affect the phase transition and reaction mechanism involved in the charge-discharge process.

3.3. Reaction mechanism

For deeper insight into the reaction mechanisms of the cation-disordered rutile-type $Li_{1.2}MnFe_{1.2}F_{6.8}$ in the IL electrolyte at 90 °C, synchrotron XRD and XPS measurements were performed on pristine electrodes and electrodes at different states of charge (SOCs), as reflected in Fig. 4, 5, and 6. A potential-time profile (Fig. 4a) highlights the SOCs of the different electrodes subjected to XRD and XPS measurements. Fig. 4b displays the XRD patterns of the $Li_{1.2}MnFe_{1.2}F_{6.8}$ electrodes at the different SOCs. The pristine electrode with a starting voltage of 3.2 V in a half-cell, which was prepared by mixing the carbon-coated $Li_{1.2}MnFe_{1.2}F_{6.8}$ with PTFE, is depicted by Pattern 1. A diffraction peak appearing around 10.4° is assigned to PTFE. This peak is retained across all patterns obtained. Rietveld fitting performed on other diffraction peaks in the pristine electrode confirms that the structure can be indexed as a cation-disordered rutile phase with the lattice parameters of a = 4.7969(9) Å and c = 3.2733(6) Å (Fig. 5a and Table S2), which is comparable with those of the carbon-coated $Li_{1.2}MnFe_{1.2}F_{6.8}$ (Fig. 1a and Table S1).

Charging the $Li_{1.2}MnFe_{1.2}F_{6.8}$ electrode to 4.5 V (Pattern 2) caused most diffraction peaks to shift to higher angles, suggesting that the delithiation resulted in a delithiated disordered rutile phase with larger a and smaller c lattice parameters than the pristine electrode (Fig. 5b

and Table S2). When the electrode was discharged to 2.5 V (Pattern 3), the diffraction pattern of the cation-disordered rutile-type $Li_{1.2}MnFe_{1.2}F_{6.8}$ was recovered, which establishes that the insertion of Li^+ into the host rutile structure is reversible (Fig. 5c and Table S2). In addition, Pattern 3 also shows new peaks assignable to LiF (space group: $Fm\bar{3}m$) and FeF_2 (space group: $P4_2/mnm$), denoting the occurrence of a partial conversion reaction from $Li_{1.2}MnFe_{1.2}F_{6.8}$ to LiF and FeF_2 in the voltage range of 2.5–4.5 V: thereby corroborating our interpretation of the charge-discharge results. Although this observation contradicts previous works on the lithium insertion mechanisms which involved the transformation of the trirutile Li*M*(II)*M*(III)F_6 phase to Li-rich phase $Li_{1+x}M(II)M(III)F_6$ at 25 °C [23-25], it is consistent with the report on the ordered trirutile $LiFe_2F_6$ investigated at 90 °C [26]. Extended discharge to 2.0 V (Pattern 4) triggered a further conversion reaction to Fe (space group: $Im\bar{3}m$) while preserving the cation-disordered rutile-type $Li_{1.2}MnFe_{1.2}F_{6.8}$, as was confirmed by the Rietveld refinement (Fig. 5d and Table S2). This conversion reaction was observed in the discharge process of iron fluorides (FeF_3 and FeF_2), even though the starting material is different from this work [40, 41]. Finally, when the electrode was recharged to 4.5 V from 2.5 V (Pattern 5), the peaks of the delithiated rutile phase were observed alongside LiF and FeF_2 peaks. This reveals that the partial conversion from the mixture of LiF and FeF_2 to the cation-disordered rutile-type $Li_{1.2}MnFe_{1.2}F_{6.8}$ occurred along with the subsequent extraction of Li^+. The lattice parameters of the delithiated phase in Pattern 5 (Fig. 5e and Table S2) bear a close resemblance to those of the delithiated phase in Pattern 2 (Fig. 5b and Table S2), which provides an attestation that the extraction/insertion of Li^+ from/into the disordered rutile-type $Li_{1.2}MnFe_{1.2}F_{6.8}$ phase is reversible.

Even though the pertinent electrochemical reactions were discerned using synchrotron XRD measurements, the oxidation states of Mn could not be ascertained due to the broad and weak diffraction peaks. Therefore, XPS measurements were performed in the Mn 3p region to

track the Mn oxidation states (see Fig. S4 for Fe 2p spectra and additional discussion). Fig. 6 shows the Mn 3p spectra at different SOCs (the spectrum number corresponds to the XRD pattern numbers). The pristine electrode (Spectrum 1) displayed a peak assignable to Mn(II) at the binding energy of 49.3 eV [42, 43]. Charging to 4.5 V (Spectrum 2) produced a peak at 49.9 eV. This peak is assigned to Mn(III) [44, 45], indicating the extraction of Li^+ from the disordered rutile-type $Li_{1.2}MnFe_{1.2}F_{6.8}$. The binding energy was seen to return to 49.3 eV upon discharge to 2.5 V (Spectrum 3), suggesting that Mn(III) was reduced to Mn(II). When the electrode was further discharged to 2.0 V (Spectrum 4), the Mn(II) peak disappeared and was replaced by a Mn(0) peak at 47.8 eV [46]. This confirms the occurrence of the further conversion reaction to LiF and metallic Mn formed by the reduction of Mn(II). Spectrum 5, obtained after the second charge from 2.5 V to 4.5 V, displayed a broad peak that can be fitted with two peaks corresponding to Mn(II) and Mn(III) at 49.3 eV and 49.9 eV, respectively. This observation not only demonstrates the partial oxidation of Mn(II) but also corroborates our conclusion from the XRD results, evincing that the second charge started to involve two redox couples: Fe(II)/Fe(III) and Mn(II)/Mn(III) which were obtained from the conversion reaction that transformed the mixture of LiF and FeF_2 to the cation-disordered rutile-type $Li_{1.2}MnFe_{1.2}F_{6.8}$.

Fig. 7 shows the schematic illustration of reaction mechanism for a Li/$Li_{1.2}MnFe_{1.2}F_{6.8}$ half-cell with the Li[FSA]-[C_2C_1im][FSA] (40:60 in mol) IL electrolyte at 90 °C. In a certain high voltage range between around 3.2 V to 4.5 V, a reversible topotactic insertion reaction is observed. This extraction/insertion reaction is proved by XPS test that it is accompanied by the Mn(II)/Mn(III) redox reaction. In a low voltage range between around 3.2 V to 2.5 V, conversion reactions from the cation-disordered rutile $Li_{1.2}MnFe_{1.2}F_{6.8}$ to rutile FeF_2, rutile MnF_2, and LiF occur along with the redox reaction of Fe(III)/Fe(II), which is marked by a change in the gradient of the discharge curve (Fig. 2a and b). Further conversion reactions to

metallic Fe, Mn and LiF occur in the low voltage ranges of 2.5–2.0 V with a characterization of a long plateau around 2.3 V (Fig. 3a and b), involving two redox reactions of Fe(II)/Fe(0), and Mn(II)/Mn(0).

4. Conclusions

This study reports for the first time a carbon-coated $Li_{1.2}MnFe_{1.2}F_{6.8}$ with cation-disordered rutile-type structure, obtained by two-step ball-milling of its stoichiometric precursors. Through a combination of charge-discharge tests in the voltage range of 2.5–4.5 V at 90 °C, synchrotron XRD and XPS analyses, we establish that the reversible topotactic extraction/insertion of Li^+ from/into $Li_{1.2}MnFe_{1.2}F_{6.8}$ cumulatively results from a synergy of redox reactions involving Mn(II)/Mn(III) and a partial conversion reaction that transforms the cation-disordered rutile $Li_{1.2}MnFe_{1.2}F_{6.8}$ to LiF and rutile FeF_2. Additionally, we ascertain that a deep discharge to 2.0 V triggers a further conversion reaction to Fe(0)/Mn(0) and LiF while preserving the cation-disordered rutile structure. Through this work, we unveil new electrochemical properties of a Li-Mn-Fe-F material with the aid of an IL electrolyte at elevated temperature. Here, we not only provide evidence of two redox couples in the electrode material but also adequately demonstrate the utilization of multiple redox couples to achieve more than 1.0 Li^+ exchange in lithium transition metal fluorides.

Declaration of Competing Interest

The authors declared that they have no conflicts of interest to this work.

Credit authorship contribution statement

Yayun Zheng: Investigation, Data curation, Writing – original draft. **Jinkwang H wang:** Writing – review & editing, Validation. **Kazuhiko Matsumoto:** Conceptualizati on, Writing – review & editing, Supervision. **Rika Hagiwara:** Funding acquisition, W

riting – review & editing, Supervision.

Acknowledgment

This study was supported by Japan Society for the Promotion of Science (JSPS, KAKENHI Grant Number 19H02811). One of the coauthors, Y. Z., thanks the China Scholarship Council (CSC) for the financial support.

Table 1. Electrochemical properties of selected Li*M*(II)*M*(III)F_6-type positive electrode materials for LIBs.

Electrodes	Synthetic methods	Electrolyte @ Temperature	1st discharge capacity @ rate	Cycling performance	Reaction mechanism	Ref.
Disordered rutile-type $LiFe_2F_6$	Ball-milling	1 M Li[PF_6]-EC:DEC @25 °C	102 mAh g^{-1} (2.5–4.0 V @9.3 mA g^{-1})	81% (17 cycles)	Reversible lithium insertion in tririutile $Li_{1+x}Fe_2F_6$	[21]
			126 mAh g^{-1} (2.0–4.5 V @9.3 mA g^{-1})	62% (14 cycles)		
Disordered rutile-type $LiMgFeF_6$	Ball-milling	1 M Li[PF_6]-EC:DEC @25 °C	Electrochemically inactive	Electrochemically inactive	Electrochemically inactive	[21]
Disordered rutile-type $Li_{1.2}Fe_2F_{6.2}$	Ball-milling	1 M Li[PF_6]-EC:DEC @25 °C	109 mAh g^{-1} (2.5–4.0 V @9.3 mA g^{-1})	84% (16 cycles)	Reversible lithium insetion	[21, 22]
			155 mAh g^{-1} (2.0–4.5 V @9.3 mA g^{-1})	88% (27 cycles)		
Trirutile $LiMgFeF_6$	Sol-gel synthesis	1 M Li[PF_6]-EC:DMC @25 °C	89 mAh g^{-1} (2–4.5 V @6.66 mA g^{-1})	120.2% (20 cycles)	Reversible lithium insertion	[23]
Trirutile $LiNiFeF_6$	Sol-gel synthesis	1 M Li[PF_6]-EC:DMC @25 °C	95 mAh g^{-1} (2–4.5 V @5.7 mA g^{-1})	92.6% (20 cycles)	Reversible lithium insertion between tririutile Li-poor $Li_{1+x1}NiFeF_6$ and tririutile Li-rich $Li_{1+x2}NiFeF_6$	[24, 25]
Trirutile $LiFe_2F_6$	Ball-milling	Li[FSA]-[C_2C_1im][FSA] (30:70 in molar)@90 °C	90 mAh g^{-1} (3.2–4.3 V @23.1 mA g^{-1})	95.4% (20 cycles)	Reversible Li extraction/insertion in two-phase manner	[26]
			175 mAh g^{-1} (2.5–4.3 V @23.1 mA g^{-1})	81.5% (20 cycles)	Reversible Li extraction/insertion and conversion reaction to LiF and rutile FeF_2	
Colquiriite-type $LiCaFeF_6$	Solid-state method	1 M Li[PF_6]-EC:DMC@25 °C	112 mAh g^{-1} (2–4.5 V @6.18 mA g^{-1})	83.9% (20 cycles)	Reversible lithium insertion	[29]
Na_2SiF_6-type $LiMnFeF_6$	Sol-gel synthesis	1 M Li[PF_6]-/EC:DMC @25 °C	95 mAh g^{-1} (2.2–4.3 V @5.78 mA g^{-1})	76.8% (10 cycles)	Reversible lithium insertion between Na_2SiF_6-type $LiMnFeF_6$ and rutile-type $Li_{1+x}MnFeF_6$	[28]

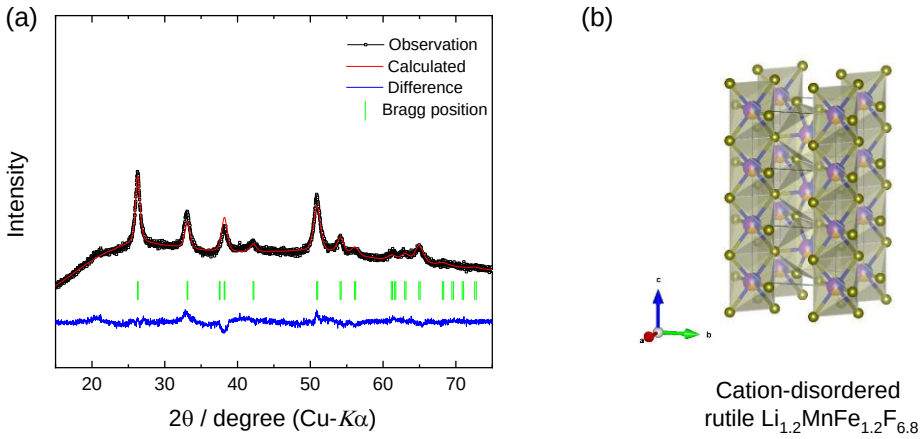

Fig. 1. (a) XRD pattern of the carbon-coated $Li_{1.2}MnFe_{1.2}F_{6.8}$ powder. (b) The refined crystal structure of the cation-disordered rutile $Li_{1.2}MnFe_{1.2}F_{6.8}$. Li, Mn, Fe, and F atoms are represented by purple, orange, blue, and green spheres, respectively. The ratio of Li, Mn, and Fe is depicted by their corresponding colors on the metal site sphere of the rutile structure.

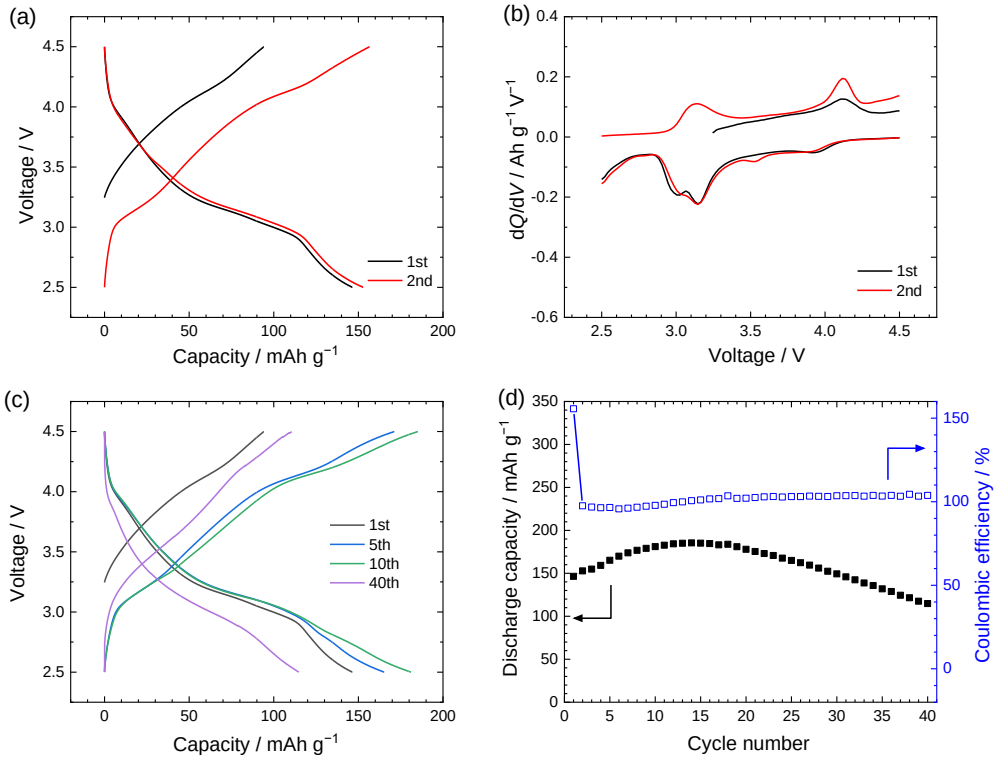

Fig. 2. Electrochemical properties of the Li/$Li_{1.2}MnFe_{1.2}F_{6.8}$ cell in the voltage range of 2.5–4.5 V at 90 °C (rate: 23.1 mA g^{-1}). (a) The 1st and 2nd charge-discharge curves and (b) their corresponding dQ/dV plots. (c) The corresponding charge-discharge curves at the 1st, 5th, 10th, and 40th cycles and (d) cycling performance during 40 cycles.

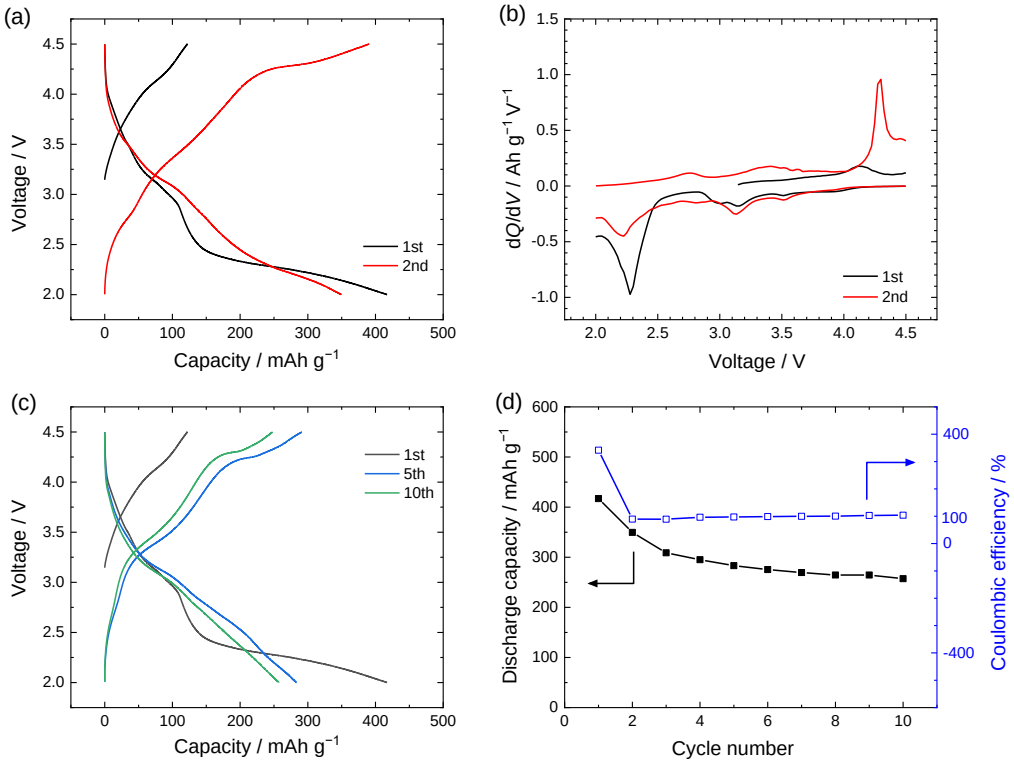

Fig. 3. Electrochemical properties of the Li/$Li_{1.2}MnFe_{1.2}F_{6.8}$ cell in the voltage range of 2.0–4.5 V at 90 °C (rate: 23.1 mA g^{-1}). (a) The 1st and 2nd charge-discharge curves and (b) their corresponding dQ/dV plots. (c) The corresponding charge-discharge curves at the 1st, 5th, and 10th cycles and (d) cycling performance for 10 cycles.

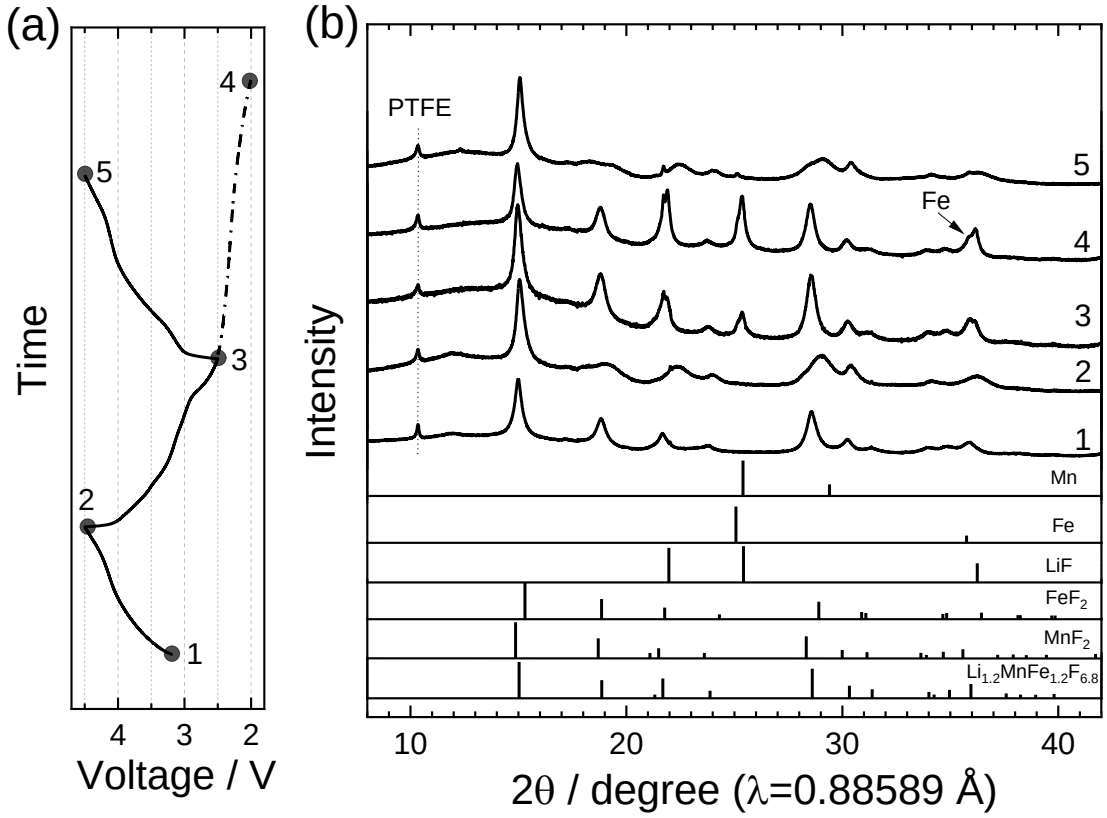

Fig. 4. (a) Charge-discharge voltage profiles of $Li_{1.2}MnFe_{1.2}F_{6.8}$ electrodes at different SOCs. The electrodes were measured (1) in the pristine state, (2) after the initial charge to 4.5 V, (3) after the initial discharge to 2.5 V, (4) after a deep discharge to 2.0 V, and (5) after the second charge to 4.5 V from the 2.5 V discharged state. (b) Ex-situ synchrotron XRD data of $Li_{1.2}MnFe_{1.2}F_{6.8}$ at different SOCs.

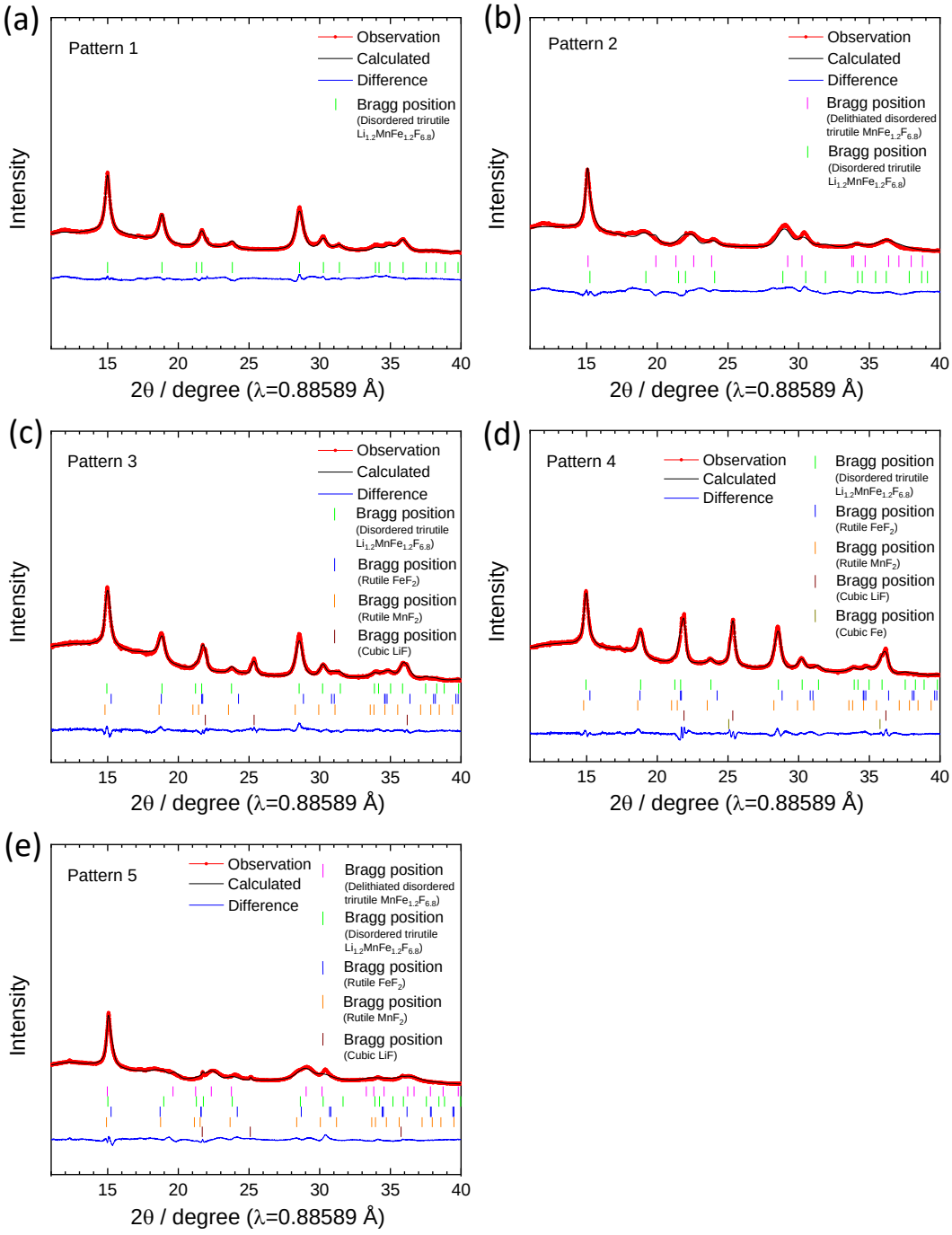

Fig. 5. Rietveld refinement results of the XRD patterns at different states of charge for the $Li_{1.2}MnFe_{1.2}F_{6.8}$ electrode. (a) Pattern 1, (b) Pattern 2, (c) Pattern 3, (d) Pattern 4, and (e) Pattern 5 corresponding to the states in Fig. 4a (refined crystallographic parameters are listed in Table S2.

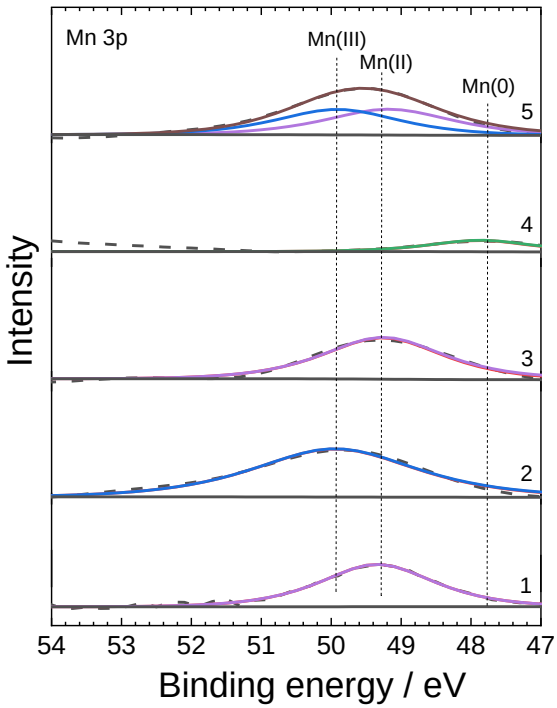

Fig. 6. The XPS spectra in the Mn 3p region of the $Li_{1.2}MnFe_{1.2}F_{6.8}$ electrodes at different SOCs corresponding to the states in Fig. 4a.

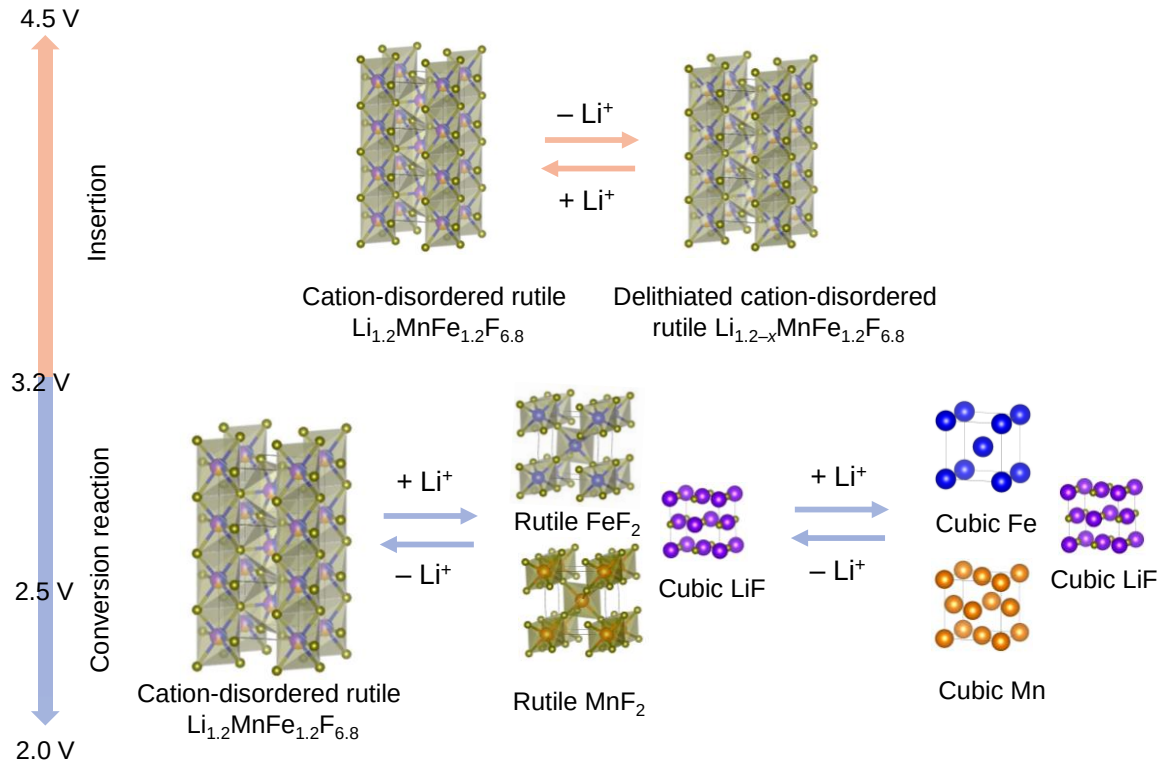

Fig. 7. The schematic illustration of reaction mechanism for a Li/$Li_{1.2}MnFe_{1.2}F_{6.8}$ half-cell with the Li[FSA]-[C_2C_1im][FSA] (40:60 in mol) IL electrolyte at 90 °C.

References

[1] H. Li, G. Richter, J. Maier, Reversible formation and decomposition of LiF clusters using transition metal fluorides as precursors and their application in rechargeable Li batteries, Adv. Mater. 15 (2003) 736−739.

[2] H. Li, P. Balaya, J. Maier, Li-storage via heterogeneous reaction in selected binary metal fluorides and oxides, J. Electrochem. Soc. 151 (2004) A1878−A1885.

[3] N. Dimov, A. Nishimura, K. Chihara, A. Kitajou, I.D. Gocheva, S. Okada, Transition metal $NaMF_3$ compounds as model systems for studying the feasibility of ternary Li-M-F and Na-M-F single phases as cathodes for lithium–ion and sodium–ion batteries, Electrochim. Acta 110 (2013) 214−220.

[4] D.E. Conte, N. Pinna, A review on the application of iron(III) fluorides as positive electrodes for secondary cells, Mater. Renew. Sustain. Energy 3 (2014) 1−22.

[5] S.K. Martha, J. Nanda, H. Zhou, J.C. Idrobo, N.J. Dudney, S. Pannala, S. Dai, J. Wang, P.V. Braun, Electrode architectures for high capacity multivalent conversion compounds: iron (ii and iii) fluoride, RSC Adv. 4 (2014) 6730–6737.

[6] C. Li, K. Chen, X. Zhou, J. Maier, Electrochemically driven conversion reaction in fluoride electrodes for energy storage devices, NPJ Comput. Mater. 4 (2018).

[7] F. Badway, F. Cosandey, N. Pereira, G.G. Amatucci, Carbon metal fluoride nanocomposites : high-Capacity reversible metal fluoride conversion materials as rechargeable positive electrodes for Li batteries, J. Electrochem. Soc. 150 (2003) A1318−A1327.

[8] F. Badway, N. Pereira, F. Cosandey, G.G. Amatucci, Carbon metal fluoride nanocomposites structure and electrochemistry of FeF_3 : C, J. Electrochem. Soc. 150 (2003) A1209−A1218.

[9] R.E. Doe, K.A. Persson, Y.S. Meng, G. Ceder, First-principles investigation of the Li-Fe-F phase diagram and equilibrium and nonequilibrium conversion reactions of iron fluorides with Lithium, Chem. Mater. 20 (2008) 5274−5283.

[10] N. Yamakawa, M. Jiang, B. Key, C.P. Grey, Identifying the local structures formed during lithiation of the conversion material, iron fluoride, in a Li ion battery: A solid-state NMR, X-

ray diffraction, and pair distribution function analysis study, J. Am. Chem. Soc. 131 (2009) 10525−10536.

[11] R.F. Li, S.Q. Wu, Y. Yang, Z.Z. Zhu, Structural and electronic properties of Li-ion battery cathode material FeF_3, J. Phys. Chem. C 114 (2010) 16813−16817.

[12] M. Zhou, L. Zhao, A. Kitajou, S. Okada, J.-i. Yamaki, Mechanism on exothermic heat of FeF_3 cathode in Li-ion batteries, J. Power Sources 203 (2012) 103−108.

[13] L. Li, F. Meng, S. Jin, High-capacity lithium-ion battery conversion cathodes based on iron fluoride nanowires and insights into the conversion mechanism, Nano Lett. 12 (2012) 6030−6037.

[14] P. Liu, J.J. Vajo, J.S. Wang, W. Li, J. Liu, Thermodynamics and kinetics of the Li/FeF_3 reaction by electrochemical analysis, J. Phys. Chem. C 116 (2012) 6467−6473.

[15] H.J. Tan, H.L. Smith, L. Kim, T.K. Harding, S.C. Jones, B. Fultz, Electrochemical cycling and lithium insertion in nanostructured FeF_3 cathodes, J. Electrochem. Soc. 161 (2014) A445−A449.

[16] A. Kitajou, I. Tanaka, Y. Tanaka, E. Kobayashi, H. Setoyama, T. Okajima, S. Okada, Discharge and charge reaction of perovskite-type MF_3 (M = Fe and Ti) cathodes for lithium-ion batteries, Electrochemistry 85 (2017) 472−477.

[17] N. Zhang, X. Xiao, H. Pang, Transition metal (Fe, Co, Ni) fluoride-based materials for electrochemical energy storage, Nanoscale Horiz. 4 (2019) 99−116.

[18] W. Viebahn, W. Rüdorff, H. Kornelson, Fluor-trirutile $LiMe^{II}Me^{III}F_6$ und zwei neue sauerstoflf-trirutile $LiMe^{V}Me^{VI}O_6$, Z. Naturforsch. B 22 (1967) 1218.

[19] V.W. Viebahn, W. Rudorff, R. Hänsler, Untersuchungen an ternären und quaternären fluoriden III: fluortrirutile und weitere lithiumhexafluorometallate, $LiMe^{II}Me^{III}F_6$, Chimia 23 (1969) 503−510.

[20] J. Kohl, D. Wiedemann, S. Nakhal, P. Bottke, N. Ferro, T. Bredow, E. Kemnitz, M. Wilkening, P. Heitjans, M. Lerch, Synthesis of ternary transition metal fluorides Li_3MF_6 via a sol–gel route as candidates for cathode materials in lithium-ion batteries, J. Mater. Chem. 22 (2012) 15819−15827.

[21] P. Liao, J. Li, J.R. Dahn, Lithium intercalation in $LiFe_2F_6$ and $LiMgFeF_6$ disordered trirutile-type phases, J. Electrochem. Soc. 157 (2010) A355−A361.

[22] P. Liao, R.A. Dunlap, J.R. Dahn, In situ mössbauer effect study of lithium intercalation in $LiFe_2F_6$, J. Electrochem. Soc. 157 (2010) A1080−A1084.

[23] G. Lieser, C. Dräger, L. de Biasi, S. Indris, H. Geßwein, S. Glatthaar, M.J. Hoffmann, H. Ehrenberg, J.R. Binder, Direct synthesis of trirutile-type $LiMgFeF_6$ and its electrochemical characterization as positive electrode in lithium-ion batteries, J. Power Sources 274 (2015) 1200−1207.

[24] G. Lieser, C. Dräger, M. Schroeder, S. Indris, L. de Biasi, H. Geßwein, S. Glatthaar, H. Ehrenberg, J.R. Binder, Sol-gel based synthesis of $LiNiFeF_6$ and its electrochemical characterization, J. Electrochem. Soc. 161 (2014) A1071−A1077.

[25] L. de Biasi, G. Lieser, J. Rana, S. Indris, C. Dräger, S. Glatthaar, R. Mönig, H. Ehrenberg, G. Schumacher, J.R. Binder, H. Geßwein, Unravelling the mechanism of lithium insertion into and extraction from trirutile-type $LiNiFeF_6$ cathode material for Li-ion batteries, CrystEngComm 17 (2015) 6163−6174.

[26] Y. Zheng, S. Tawa, J. Hwang, Y. Orikasa, K. Matsumoto, R. Hagiwara, Phase evolution of trirutile $Li_{0.5}FeF_3$ for lithium-ion batteries, Chem. Mater. 33 (2021) 868−880.

[27] G. Courbion, C. Jacoboni, R.D. Pape, The dimorphism of $LiMnFeF_6$: a new kind of cationic order in the structural type Na_2SiF_6, J. Solid State Chem. 45 (1982) 127−134

[28] G. Lieser, L.d. Biasi, H. Geßwein, S. Indris, C. Dräger, M. Schroeder, S. Glatthaar, H. Ehrenberg, J.R. Binder, Electrochemical characterization of $LiMnFeF_6$ for use as positive electrode in lithium-ion batteries, J. Electrochem. Soc. 161 (2014) A1869−A1876.

[29] L. de Biasi, G. Lieser, C. Dräger, S. Indris, J. Rana, G. Schumacher, R. Mönig, H. Ehrenberg, J.R. Binder, H. Geßwein, $LiCaFeF_6$: A zero-strain cathode material for use in Li-ion batteries, J. Power Sources 362 (2017) 192−201.

[30] T. Sekino, T. Endo, T. Sato, M. Shimada, High-pressure synthesis of $LiTiMF_6$ (M = Mn, Fe, Co, Ni) with trirutile, Na_2SiF_6, and $PbSb_2O_6$ structures, J. Solid State Chem. 88 (1990) 505−512.

[31] X. Lin, M. Salari, L.M. Arava, P.M. Ajayan, M.W. Grinstaff, High temperature electrical energy storage: advances, challenges, and frontiers, Chem. Soc. Rev. 45 (2016) 5848−5887.

[32] M.-T.F. Rodrigues, G. Babu, H. Gullapalli, K. Kalaga, F.N. Sayed, K. Kato, J. Joyner, P.M. Ajayan, A materials perspective on Li-ion batteries at extreme temperatures, Nat. Energy 2 (2017) 1−14.

[33] J. Hwang, K. Matsumoto, R. Hagiwara, $Na_3V_2(PO_4)_3$/C positive electrodes with high energy and power densities for sodium secondary batteries with ionic liquid electrolytes that operate across wide temperature ranges, Adv. Sustainable Syst. 2 (2018) 1−11.

[34] B.H. Toby, EXPGUI, a graphical user interface for GSAS, J. Appl. Cryst. 34 (2001) 210−213.

[35] K. Momma, F. Izumi, VESTA 3 for three-dimensional visualization of crystal, volumetric and morphology data, J. Appl. Crystallogr. 44 (2011) 1272−1276.

[36] T. Torimoto, T. Tsuda, K. Okazaki, S. Kuwabata, New frontiers in materials science opened by ionic liquids, Adv. Mater. 22 (2010) 1196−1221.

[37] D.R. MacFarlane, N. Tachikawa, M. Forsyth, J.M. Pringle, P.C. Howlett, G.D. Elliott, J.H. Davis, M. Watanabe, P. Simon, C.A. Angell, Energy applications of ionic liquids, Energy Environ. Sci. 7 (2014) 232−250.

[38] K. Matsumoto, E. Nishiwaki, T. Hosokawa, S. Tawa, T. Nohira, R. Hagiwara, Thermal, physical, and electrochemical properties of $Li[N(SO_2F)_2]$-[1-Ethyl-3-methylimidazolium][$N(SO_2F)_2$] ionic liquid electrolytes for Li secondary batteries operated at room and intermediate temperatures, J. Phys. Chem. C 121 (2017) 9209−9219.

[39] J. Hwang, H. Okada, R. Haraguchi, S. Tawa, K. Matsumoto, R. Hagiwara, Ionic liquid electrolyte for room to intermediate temperature operating Li metal batteries: Dendrite suppression and improved performance, J. Power Sources 453 (2020) 1−6.

[40] L. Li, R. Jacobs, P. Gao, L. Gan, F. Wang, D. Morgan, S. Jin, Origins of large voltage hysteresis in high-energy-density metal fluoride lithium-ion battery conversion electrodes, J. Am. Chem. Soc. 138 (2016) 2838−2848.

[41] A.W. Xiao, H.J. Lee, I. Capone, A. Robertson, T.U. Wi, J. Fawdon, S. Wheeler, H.W. Lee, N. Grobert, M. Pasta, Understanding the conversion mechanism and performance of monodisperse FeF_2 nanocrystal cathodes, Nat. Mater. 19 (2020) 644−654.

[42] A. Aoki, X-ray photoelectron spectroscopic studies on ZnS: MnF_2 phosphors, J. Appl. Phys. 15 (1976) 305−311.

[43] X. Xiao, Z. Liu, L. Baggetto, G.M. Veith, K.L. More, R.R. Unocic, Unraveling manganese dissolution/deposition mechanisms on the negative electrode in lithium ion batteries, Phys. Chem. Chem. Phys. 16 (2014) 10398−10402.

[44] G. Fortunato, H.R. Oswald, A. Reller, Spinel-type oxide catalysts for low temperature CO oxidation generated by use of an ultrasonic aerosol pyrolysis process, J. Mater. Chem. 11 (2001) 905−911.

[45] K.M. Shaju, K.V. Ramanujachary, S.E. Lofland, G.V. Subba Rao, B.V.R. Chowdari, Spectral, magnetic and electrochemical studies of layered manganese oxides with P_2 and O_2 structure, J. Mater. Chem. 13 (2003) 2633−2640.

[46] A.R. Chourasia, D.R. Chopra, Elemental manganese studied by X-ray photoemission spectroscopy using Mg and Zr radiations, Surf. Sci. Spectra 3 (1994) 74−81.